Lagrangian Coherent Structures near a Subtropical Jet Stream

WENBO TANG

School of Mathematical and Statistical Sciences, Arizona State University, Tempe, Arizona

MANIKANDAN MATHUR AND GEORGE HALLER*

Department of Mechanical Engineering, Massachusetts Institute of Technology, Cambridge, Massachusetts

DOUGLAS C. HAHN[+] AND FRANK H. RUGGIERO

Air Force Research Laboratory, Hanscom Air Force Base, Massachusetts

ABSTRACT

Direct Lyapunov exponents and stability results are used to extract and distinguish Lagrangian coherent structures (LCS) from a three-dimensional atmospheric dataset generated from the Weather Research and Forecasting (WRF) model. The numerical model is centered at 19.78°N, 155.55°W, initialized from the Global Forecast System for the case of a subtropical jet stream near Hawaii on 12 December 2002. The LCS are identified that appear to create optical and mechanical turbulence, as evidenced by balloon data collected during a measurement campaign near Hawaii.

1. Introduction

In this paper we seek to identify Lagrangian coherent structures (LCS) in a three-dimensional unsteady atmospheric flow field. The wind field was generated by the Weather Research and Forecasting (WRF) model, initialized from the Global Forecast System (GFS). Our objective is to provide a physically objective (i.e., frame-independent) identification of the aerial structures that create mechanical and optical turbulence in this flow.

Coherent structures have been studied extensively in several areas of geophysical fluid dynamics. Galilean-invariant definitions of coherent vortices exist, typically yielding different results when applied to the same flow. For example, Chong et al. (1990) define vortices as regions where velocity gradient admits complex eigenvalues. Alternatively, Jeong and Hussain (1995) use the intermediate eigenvalue of the velocity gradient tensor to identify regions of vortical motion. Andreassen et al. (1998) and Gushchin and Matyushin (2006) use this method to identify vortex formation in breaking internal gravity waves and wake flows behind a sphere. As discussed in Haller (2005), a shortcoming of these coherent structure detection schemes is their dependence on the frame of reference used in the study.

Perhaps the simplest example illustrating this frame dependence is the following. Define a coherent vortex in a two-dimensional flow as a region filled with closed instantaneous streamlines. Such regions will exist in the frame of one observer (e.g., a person standing on a beach) but disappear in a frame attached to another observer (e.g., a person traveling on an airplane). Another example is the well-known Okubo–Weiss criterion (Okubo 1970; Weiss 1991) that identifies a vortex as a region where vorticity exceeds the rate of strain. It is not hard to see that vortices defined in such a fashion may appear or disappear in appropriate rotating frames as the rotation of the frame increases or decreases vorticity. For most geophysical applications, even though the reference frame is attached to the earth, Galilean-invariant

---

* Current affiliation: Department of Mechanical Engineering, McGill University, Montreal, Quebec, Canada.
[+] Current affiliation: Air Force Weather Weapon System, Hanscom Air Force Base, Massachusetts.

Corresponding author address: George Haller, Department of Mechanical Engineering, McGill University, Montreal QC H3A 2 K6, Canada.
E-mail: george.haller@mcgill.ca

criteria mentioned above can still give contradictory results, as shown in Haller (2005) and in section 3 for the particular case studied here, making the selection of these criteria difficult and the results arbitrary. This is because changes of a nonlinear feature in an unsteady flow may be a feature of the frame instead of a feature in the physical flow. To ensure physical objectivity in continuum mechanics, any newly proposed constitutive law or flow quantity must be fully frame independent to be considered intrinsic to the properties of the moving continuum.

For the above reasons, here we select a Lagrangian (i.e., particle-based) approach to coherent structure detection. Because the mathematical tool we use is material-based, this approach is inherently frame independent. Specifically, we compute the finite-time Lyapunov exponent field associated with the flow directly from the advection of a regular initial grid of infinitesimal particles. Maximal lines/surfaces (ridges) of the resulting direct Lyapunov exponent (DLE) field computed from forward-time particle trajectories have been shown to mark distinct material surfaces that repel all nearby fluid particles; we therefore refer to such ridges as repelling LCS. Similar ridges obtained from a backward-time DLE analysis mark distinct attracting material surfaces; we refer to such ridges as attracting LCS.

Local maxima of shear also appear as DLE ridges, even though they do not induce exponential separation of particles. To distinguish these shear-type LCS from hyperbolic (i.e., attracting or repelling) LCS, we use stability results from Haller (2002). Shear-type LCS turn out to play an important role in the present flow, as these LCS act as Lagrangian boundaries of a subtropical jet stream.

The dataset we analyze here contains high-resolution three-dimensional numerical weather prediction simulations combined with in situ balloon measurements. This enables us, for the first time, to analyze directly the role of LCS in depicting wind patterns and turbulence. Our goal is to develop a mathematical and numerical tool to accurately extract and distinguish from a velocity dataset the coherent structures that are responsible for different types of clear-air turbulence. Prior studies of coherent structures and its relations to atmospheric turbulence include the interaction of topographically generated gravity waves with upper-level jets (Clark et al. 2000), the generation and breaking of inertia–gravity waves by an upper-level jet (Lane et al. 2004; Koch et al. 2005; Lu and Koch 2008), and the structure of the wake behind isolated obstacles (Hunt and Snyder 1980; Smolarkiewicz and Rotunno 1989; Rotunno and Smolarkiewicz 1991). We use LCS to objectively identify flow organized by the aforementioned coherent motions—they are the actual material structures of the flow that form the skeleton of turbulence (Mathur et al. 2007).

Beyond comparison with Eulerian coherent vortex identifications, we also compare LCS with standard turbulent diagnosis using the Richardson number. These comparisons provide us with better understandings of the applicability and fidelity of LCS in the objective detection of locations of atmospheric turbulence.

This paper is organized as follows: in section 2 we describe the WRF data used in our analysis; in section 3 the DLE field is computed from velocity data in the WRF and compared with Eulerian flow diagnostics. We also discuss the Lagrangian flow topology based on LCS extracted from DLE. In section 4 we focus on the interior of the jet stream from the case mentioned above and identify the stability type of the structures within the jet, in section 5 we compare the extracted LCS with balloon measurements of turbulence, and in section 6 we summarize our results and present some concluding remarks.

2. The WRF data

The atmospheric dataset analyzed here was generated by the WRF modeling system using the Advanced Research WRF (ARW) version 2 dynamics solver core (Skamarock et al. 2005). The model was initialized with global 1° latitude/longitude analysis data from the Global Forecast System, which is run twice daily by the National Centers for Environmental Prediction (NCEP), part of the U.S. National Weather Service (NWS). Mercator projection was used for this forecast.

The ARW-WRF was configured using 81 vertical layers and four horizontally nested grids with an innermost grid resolution of 1.3 km. The model top was limited to an atmospheric pressure of 10 hPa. Forecast data from the third nest, at a resolution of 4 km, was output every time step of the simulation (20 s) for this study. The innermost grid was used to benefit the 4-km domain using two-way feedback from the nests and the third nest is analyzed because of the large file sizes used for Lagrangian integration. The WRF simulation was run for a 24-h forecast beginning at 1200 UTC 11 December 2002. The latter half of the data (between 0000 and 1200 UTC 12 December 2002) was used in our analysis.

Subgrid-scale physical parameterizations of short-wave and longwave radiation, the surface and boundary layer, microphysics, and cumulus convection were used in each WRF model nest except in the innermost nest where the fine grid resolution allowed convection to be explicitly resolved. A subgrid-scale turbulence parameterization was unnecessary since the horizontal grid sizes in all nests were not small enough to require one. As such, we use the Yonsei University (YSU) PBL parameterization
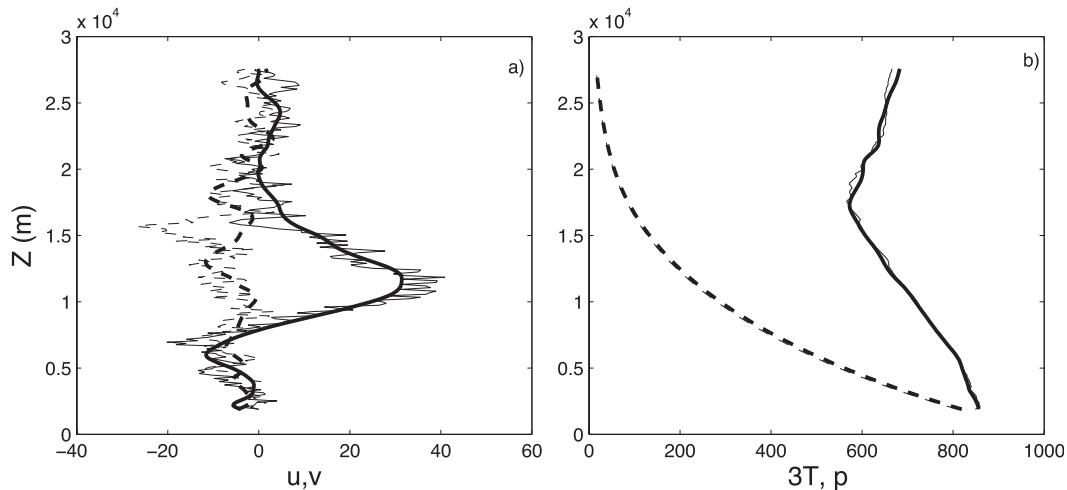
FIG. 1. Comparison between balloon measurements for the thermosonde balloon released at 0657 UTC and model outputs. (a) Zonal (solid curves) and meridional (dashed curves) velocities (m s^{-1}). (b) Temperature (K, solid curves, enlarged 3 times to show details) and pressure (hPa, dashed curves). For both panels, the thick curves are model outputs and the thin curves are balloon measurements.

scheme to resolve the vertical subgrid-scale fluxes due to eddy transports. The horizontal eddy viscosity κ_h was determined from the horizontal deformation using a Smagorinsky first-order closure approach. Boundary conditions were imposed on the model grid domains to minimize reflections of internal waves at the boundaries. Diffusive dampening was applied at the top boundary to absorb gravity waves with a damping layer depth of 5 km and a nondimensional damping coefficient of 0.01. Vertical velocity damping was also used to stabilize the forecast. GFS analyses were used to provide boundary conditions for the outermost grid with two-way feedback used for adjacent inner WRF grids.

Figure 1 shows the comparison between the model output and data collected from the thermosonde balloon released at 0657 UTC. In Fig. 1a the horizontal velocities are shown. Except for around $z = 15$ km, when the model fails to capture a meridional velocity spike, the model outputs capture the horizontal velocity components fairly well. The pressure (hPa) and temperature (K) comparisons are shown in Fig. 1b. Temperature has been enlarged three times to reveal fine details. Again, the model outputs are nearly indistinguishable from the balloon measurements.

3. Direct Lyapunov exponents and flow topology

Before introducing the DLE (or finite-time Lyapunov exponent) we first use different Eulerian diagnoses to analyze the model data. Figure 2 shows a comparison between these diagnostics. In Fig. 2a, the Okubo–Weiss criterion (Okubo 1970; Weiss 1991) is shown for the

vertical cut of $x = 0$ km. Regions in red are identified as vortices and regions in blue are strains. Figure 2b shows the Δ criterion described in Chong et al. (1990). Vortex regions and strain regions have the same color as Fig. 2a. There is some resemblance of the structures in Fig. 2b compared to the Okubo–Weiss criterion in Fig. 2a because the Okubo–Weiss criterion is directly used when computing for Δ. Figure 2c shows the vortex criterion proposed by Jeong and Hussain (1995). The color scheme for vortex and strain are the same as Figs. 2a,b. The structures are already different from the other criteria. For a detailed discussion of comparisons among these criteria see Haller (2005). Finally in Fig. 2d we show the conventional diagnostic for shear instability—the gradient Richardson number Ri, which is filtered to be between 0 and 1 to highlight unstable regions. It is seen that Ri $< \frac{1}{4}$ only in very limited regions at about $z = 10$ km. We will see later in this section that those regions correspond to the core of a jet stream, with the presence of Kelvin–Helmholtz (K-H) billows. As seen in this figure, the vortex criteria specifically targeted at identifying coherent structures reveal different results, whereas the conventional criterion—the Richardson number—only indicates instability in isolated regions. We will see that the DLE reveals coherent structures in this flow with more detail, and inherently there is no ambiguity because of the Lagrangian framework we are in.

The DLE computed for an initial position in the flow measures the largest rate of stretching along the trajectory starting from that position. More specifically, let $\mathbf{v}(\mathbf{x}, t)$ denote the velocity field associated with the atmospheric
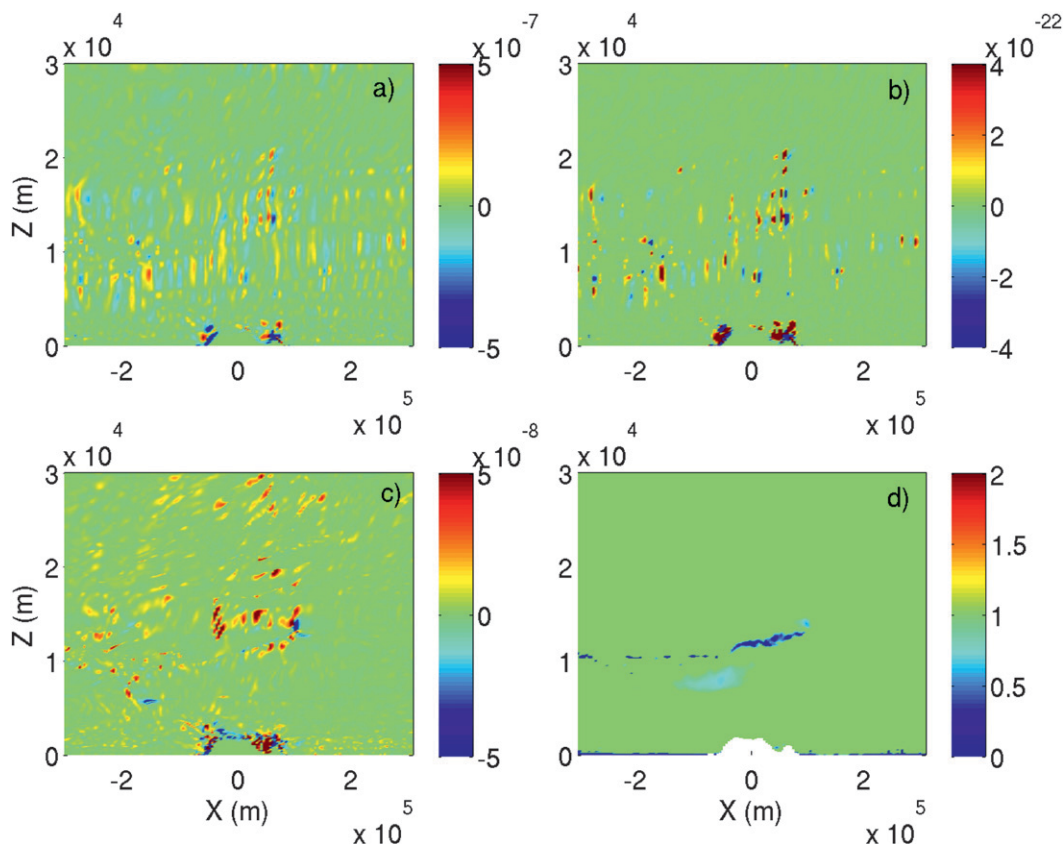
FIG. 2. Comparison between Eulerian coherent structures and traditional diagnostics: (a) Okubo–Weiss criterion, (b) Δ criterion by Chong et al. (1990), (c) λ_2 criterion by Jeong and Hussain (1995), and (d) gradient Richardson number Ri. In (a)–(c) regions in red indicate vortices and regions in blue indicate strain. In (d), Ri has been filtered to be between 0 and 1 to reveal the most important structures.

flow field. A fluid trajectory $\mathbf{x}(t)$ starting from $\mathbf{x}_0$ at time t_0 satisfies the differential equation

$$\dot{\mathbf{x}}(t) = \mathbf{v}[\mathbf{x}(t), t], \quad \mathbf{x}(t_0) = \mathbf{x}_0. \quad (1)$$

The Cauchy–Green strain tensor field is defined as

$$\mathbf{M}_{t_0}^t(\mathbf{x}_0) \equiv \left[\frac{\partial \mathbf{x}(t; \mathbf{x}_0, t_0)}{\partial \mathbf{x}_0} \right]^{\mathrm{T}} \left[\frac{\partial \mathbf{x}(t; \mathbf{x}_0, t_0)}{\partial \mathbf{x}_0} \right],$$

where $\mathbf{x}(t; \mathbf{x}_0, t_0)$ is the time t position of the trajectory that starts from $\mathbf{x}_0$ at time t_0, and $[\partial \mathbf{x}/\partial \mathbf{x}_0]^{\mathrm{T}}$ denotes the transpose of the deformation gradient tensor $\partial \mathbf{x}/\partial \mathbf{x}_0$. The DLE field, $\mathrm{DLE}_{t_0}^t(\mathbf{x}_0)$, is then defined as the scalar field that associates with each initial position $\mathbf{x}_0$ the maximal rate of stretching along $\mathbf{x}(t; \mathbf{x}_0, t_0)$:

$$\mathrm{DLE}_{t_0}^t(\mathbf{x}_0) = \frac{1}{2(t - t_0)} \log \lambda_{\max}(M),$$

with $\lambda_{\max}(M)$ denoting the maximum eigenvalue of M.

As shown in Haller (2001, 2002), ridges of $\mathrm{DLE}_{t_0}^t(\mathbf{x}_0)$ mark the time t_0 position of material surfaces that repel

nearby fluid trajectories at locally the highest rate in the flow over the time interval $[t_0, t]$. We call these surfaces repelling Lagrangian coherent structures (repelling LCS). Similarly, for $t < t_0$, ridges of $\mathrm{DLE}_{t_0}^t(\mathbf{x}_0)$ mark the time t_0 position of material surfaces that attract nearby trajectories at locally the highest rate in the flow over the time interval $[t, t_0]$. We call these surfaces attracting LCS. As the base time t_0 is varied, LCS extracted for different t_0 turn out to be advected into one another by the fluid velocity (i.e., DLE ridges are near-material lines; Shadden et al. 2005).

To compute the DLE field described above, we integrate trajectories in a Cartesian coordinate system. To achieve this, we use linear interpolation to change from the pressure coordinate into 85 uniformly spaced grids in height. The top boundary of the domain, of 10 hPa in pressure, corresponds to roughly 30 km in altitude. The horizontal velocities from the spherical coordinate are then mapped onto Cartesian grids using the Mercator projection. The size of the horizontal domain in the Cartesian coordinate is 620 km × 620 km. Fluid particle

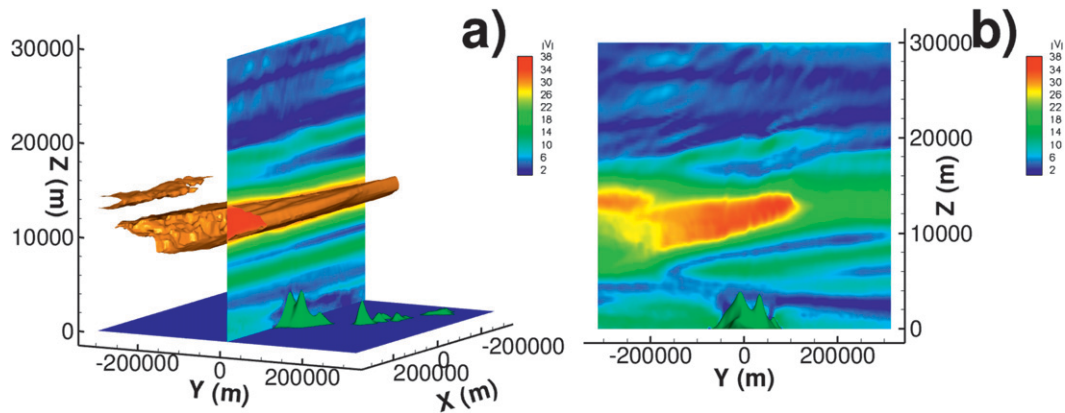FIG. 3. The horizontal velocity $|\mathbf{v}_H|$ at 0530 UTC. Large velocity is marked in red, indicating a jet stream aloft around $z = 12$ km. (a) Three-dimensional view similar to Fig. 4. Contour legend is the velocity (m s^{-1}). (b) Vertical section at $x = 0$ km. Contour legend is as in Fig. 3a.

trajectory integration is then performed by solving Eq. (1) using a fourth-order Runge–Kutta scheme with linear interpolation in time and space.

Since velocity is unspecified outside the model domain, we choose to stop advecting fluid particles once they reach the boundaries of the domain. To minimize the impact of this procedure on the extracted LCS, we choose the time of integration so that most fluid particles stay within the domain. Specifically, we select $T = t - t_0 = 4$ h, that is, roughly 80% of the time that the fastest-moving fluid particles inside the jet stream will travel across the computational domain. As a result, about 20% of the trajectories inside and most trajectories outside the jet stream are unaffected by the artificial boundary condition we impose. With this integration time, every DLE field comprises 720 frames of instantaneous velocity information. This choice of integration time also allows for a 4-h time window from the 12-h dataset within which we can study the evolution of the extracted structures in both forward and backward time.

We focus on a window of analysis between 0500 and 0800 UTC since it corresponds to the flight time of the first two balloons during the measurement campaign. Comparisons between the LCS extracted in this section and campaign measurements will be given later.

Figure 3 shows the location of the jet stream in the domain of interest. An isosurface of the horizontal velocity at 32 m s^{-1} has been plotted in Fig. 3a along with a streamwise transection of this field at $y = 0$ km (constant latitude plane at 19.78°N). Figure 3b shows the spanwise transection at $x = 0$ km (constant longitude plane at 155.55°W). The jet stream is bounded roughly between $z = 6$ km and $z = 17$ km, as its thickness changes with horizontal coordinates. There are some fine structures in the center of the jet above the

islands and the intensity of the jet diminishes toward the left (north).

Figure 4 shows the forward-time and backward-time DLE fields at base time $t_0 = 0530$ UTC, when the first balloon reaches the jet stream. The x and y coordinates correspond to the zonal and meridional directions in a spherical coordinate system, respectively. For visual convenience, we have chosen a viewing angle from the east-northeast of the domain, so that the jet stream runs from the back to the front toward the reader's left.

The LCS are shown as locally maximum isosurfaces in the DLE fields. We also plot the color contours on one vertical slice of the three-dimensional domain to aid the interpretation of the structures. The unit for the color contours in these plots is min^{-1}; regions in red denote high values of DLE corresponding to constant DLE values of 0.019 min^{-1} and the vertical slice corresponds to a constant latitude plane at 19.78°N, or the $y = 0$ km plane in our coordinate (positive x points east and positive y points north).

The LCS in Fig. 4 can be divided into three primary regions based on altitudes. The first (and dominant) region is the subtropical jet stream whose core is roughly between $z = 10$ km and $z = 15$ km. The second region is above the jet dominated by gravity waves. The third region is below the jet dominated by the east-northeast trade flow.

a. Jet stream region

The jet stream structure is bounded by two big layers of large DLE (in both forward and backward time), revealed by the isosurfaces, corresponding to the upper and lower jet boundaries. Large separation of fluid particles corresponds to the strong shear created from the interaction between the jet and ambient flows above and below.
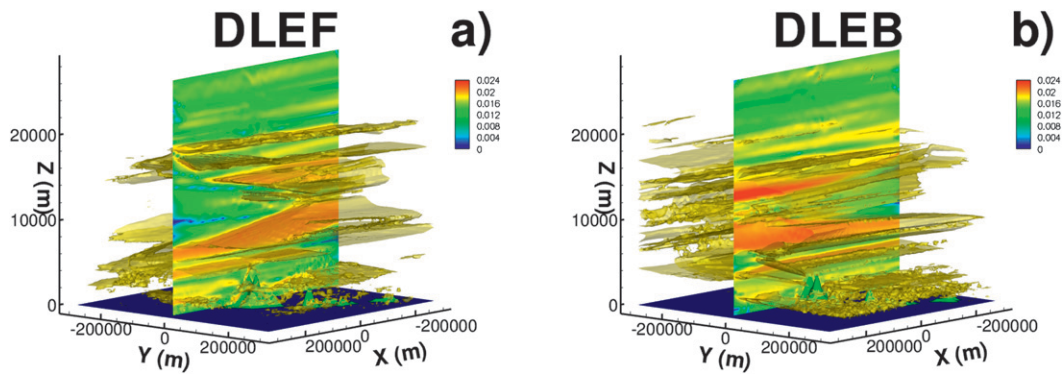
FIG. 4. Depictions of the DLE fields at 0530 UTC corresponding to the plot shown in Fig. 3a. (a) The forward-time DLEs (DLEF) depicting regions of large forward-time particle separation, corresponding to repelling structures and strong shear. (b) The backward-time DLEs (DLEB) depicting regions of large backward-time particle separation, corresponding to attracting structures and strong shear. Large values of DLE are colored in red; lower values are indicated by blue. The unit in the legend for the color contours is min^{-1}. The vertical plane corresponds to a constant latitude slice at 19.78°N.

Inside the jet stream, we also observe some fine LCS aligned with the jet, at around $z = 12$ km. In Fig. 4a, these structures appear to be in the upstream end of the jet, whereas in Fig. 4b they appear at the downstream end (or ''upstream'' end in backward time). Figure 5 reveals the inner structures with more clarity. Figure 5a shows the horizontal cut of the forward-time DLE field at $z = 12$ km, whereas Fig. 5b shows the vertical cut of the same DLE field at $x = 0$ km—a transection of the jet stream. The two black lines in these figures indicate the intersection of the two planes. The fine structures inside the jet stream appear to be a series of six ridges in the color contour in the upper half of Fig. 5a. The ridges are

roughly 25 km apart from each other and hence are true flow features resolved by the numerical model.

In Fig. 5b, we find that the transection of the fine structures appear to be an array of S-shaped objects packed in the jet core. These objects are outlined by the black curves in the figure. As we show in the next section, these structures correspond to the boundaries of a series of vortex rolls (K-H billows due to shear instability) above Hawaii, indicating that the jet is bounded, between $z = 6$ km and $z = 17$ km, with DLE, encapsulating the inner structures seen in the figure. In fact, the fine structures in the jet core of Fig. 3b also show these K-H billows, but LCS reveal them with higher
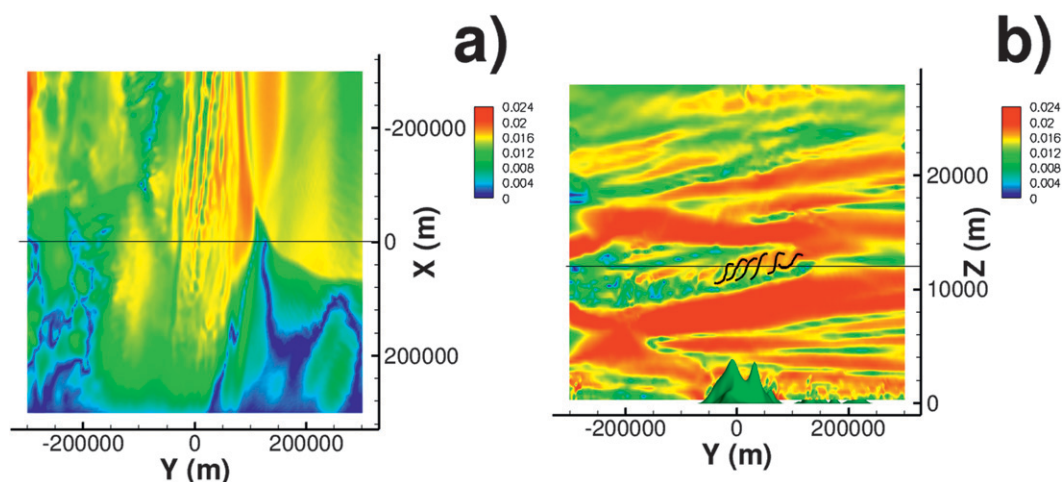

FIG. 5. Horizontal and vertical cuts of the DLEF at 0530 UTC. The same cuts are shown in Fig. 4a for the fine structures inside the jet stream. (a) Horizontal cut at $z = 12$ km. (b) Vertical section at $x = 0$ km. The S-shaped structures are highlighted by the series of black curves. They arise from shear instability between velocity vectors in the jet core and at the base of the gravity wave region. Contour legend is as in Fig. 4a.

clarity. At lower latitudes (toward the left of the jet core in Fig. 5b), the structures inside the jet stream spread out from vortex rolls to more complicated structures. From the horizontal velocity plot in Fig. 3b, we also see that the intensity of the jet stream is diminished toward the left. We note that the highlighted regions inside the jet are the most unstable regions in the jet core, whereas the quieter regions see less relative motion of air particles—hence less mixing and turbulence.

b. Region above the jet

Above the upper jet boundary, we enter the second main region of flow behavior. As shown in McHugh et al. (2008), the tropopause is around $z = 17$ km, above which density stratification become much stronger. With increasing height, the wind direction changes significantly from the zonal jet into a helical flow. In fact the big red layer above the green jet core in Fig. 5b depicts this strong directional wind shear—fluid particle trajectories starting inside the green jet core region is advected zonally, whereas trajectories starting immediately above the jet core inside the red upper boundary region are caught with the helical flow and separate far away from their neighbors, leaving the red signature in the DLE field. The helical flow structure starting from the upper jet boundary corresponds to a region of gravity waves triggered by the jet stream, with smaller DLE values due to less nonlinearity. The gravity wave structure is better revealed with a plot of potential temperature anomalies (not shown). Although DLE values here are not large, we can still infer the gravity wave structure from Fig. 5b—the peaks and troughs of the DLE field reveal the orientation of the waves. Indeed, the strong directional shear at the base of this helical flow may be conducive to the generation of the K-H billows in the jet core as well. Prior studies (Clark et al. 2000; Lane et al. 2004; Koch et al. 2005; Lu and Koch 2008) indicate that jet–gravity wave interactions are prone to production of clear-air turbulence. Here the LCS reveal material structures that experience the strongest nonlinear motion in this region—likely candidates for clear-air turbulence.

c. Region below the jet

The third main region is below the lower jet boundary, where the east-northeast trade flow dominates. A turbulent wake induced by the trade flow over and around Hawaii is captured by the DLE field. Lane et al. (2006); Porter et al. (2007) discuss wake structures of atmospheric flows in these regions. In Fig. 6, we show the corresponding structures by isosurfaces of the forward-time DLE field at 0.185 min^{-1} and a horizontal slice at $z = 700$ m, corresponding roughly to the 925-hPa level.
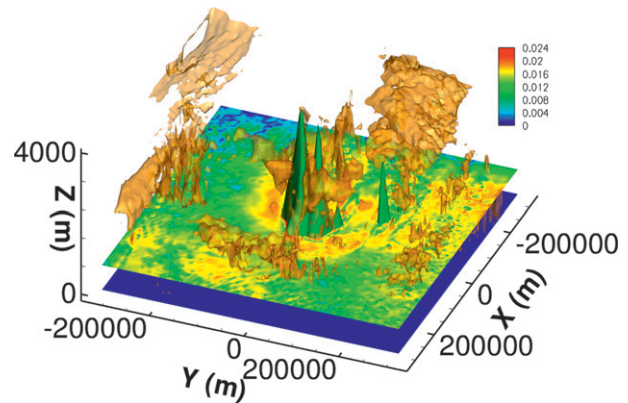

FIG. 6. A horizontal cut of the DLEF at $z = 700$ m and isosurfaces of 0.185 min^{-1} showing a wake in the lee of the Big Island. This is due to the trade flow coming from the east-northeast passing over island topography. Notice that the vertical scale has been enlarged in this plot.

Vertical structures in the wake are seen from the isosurfaces. Away from the islands, we also see some high values of the forward-time DLE in the horizontal cut. Large DLE values are due to high nonlinearity of the trajectories, signaling chaotic flow behavior within the boundary layer. Note that the vertical coordinate has been stretched as compared to other figures in order to enhance the structures.

We have also computed the DLE fields at 0730 UTC (not shown in this section). The coherent structures revealed by those DLE computations show only small variations from those in Fig. 4. We will discuss them in the context of evolution of structures and comparison with balloon measurements in the next two sections.

In the following section, we give a detailed analysis of the most influential LCS and their evolution within the jet stream. Analysis of LCS in other regions can be carried out in the same manner.

4. Extraction and classification of Lagrangian coherent structures

DLE ridges highlight intense separation of fluid particle trajectories; such separation may be the result of exponential instability (hyperbolic LCS) or strong shear (parabolic LCS). To differentiate between hyperbolic and parabolic LCS, we will use the LCS stability results proved in Haller (2001).

a. Numerical extraction of LCS

To locate LCS as DLE ridges, we use the second-derivative ridge definition described in Shadden et al. (2005) and Lekien et al. (2007) and require that 1) the normal of the ridge must be parallel to the local DLE
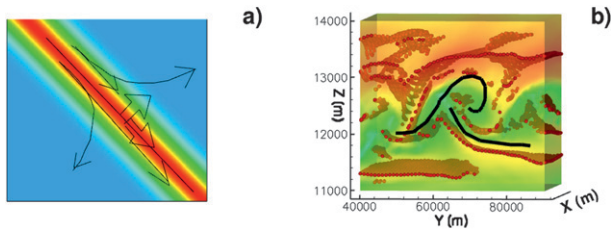
FIG. 7. (a) Illustration of a 2D ridge extraction. The gradient vector and the eigenvector associated with the negative eigenvalue of the second-derivative matrix are orthogonal on the ridge. Black trajectories with small arrows indicate fluid particle motion near an LCS in different coherent types. (b) Ridge extraction near a vortex roll at 0200 UTC. The color contour is the DLEF; the red spheres lie along the ridges of this field. The "R" shape is highlighted by the black curves.

gradient and 2) the second-order derivative of the DLE along the ridge must have at least one negative eigenvalue.

Since the DLE gradient along a ridge is parallel to the ridge, ridges can be, in principle, extracted as the zero isocontour/surface of the product of the eigenvector associated with the minimum (negative) eigenvalue from the second-derivative matrix and the DLE gradient (Shadden et al. 2006). This approach, however, is only effective for well-pronounced and connected ridges, neither of which is the case for our dataset.

Instead, we extract DLE ridges in a manner analogous to the technique employed by Mathur et al. (2007) for two-dimensional flows. In particular, we advect a set of tracers under the DLE gradient field. The initial conditions are considered to be close to the ridge if the product of the gradient and the eigenvector associated with the negative eigenvalue is close to zero. Once this is satisfied, tracers are further advected toward the ridge under the eigenvector field (corresponding to the negative eigenvalue). In this fashion we avoid moving initial conditions toward summits along the ridges so ridge extraction is more efficient. To avoid extracting saddle points that have steeper valleys than ridges, we further require that the "ridgeness" (i.e., the minimal eigenvalue) be greater in magnitude than the "valleyness" (i.e., the maximal eigenvalue).

In Fig. 7a we illustrate the idea of ridge extraction for a 2D scalar field. The ridgeline (black line) is the maximal line that separates flow (initial conditions) into different basins. Locally on the ridgeline, the gradient vector is along the ridge, and the requirement of a negative eigenvalue of the second-derivative matrix ensures that the scalar is at its maximum in the direction that is perpendicular to the ridge. The eigenvector associated with this negative eigenvalue is perpendicular to the ridge, so we arrive at the two conditions listed above.

The black trajectories with arrows in Fig. 7a are reserved for discussion in the next subsection.

As a result of this procedure, Fig. 7b shows DLE ridges represented as surfaces of accumulated tracers where the above-stated ridge criteria are met.

The color contour in Fig. 7b refers to the forward-time DLE field. The extracted LCS are represented by the red spheres embedded in the plot. In this subdomain, we see one complete vortex roll in the jet core. The vortex roll structure is outlined as an "R" shape by the ridge surfaces, connecting to neighboring vortices through openings at the bottom. As we show in Fig. 8, these ridge surfaces organize the entrainment and detrainment of fluid blobs near the vortex center at around $y = 68$ km and $z = 12.6$ km.

b. Classification of LCS

To classify the extracted LCS as hyperbolic or parabolic, we compute the strain rate normal and tangential to the ridge surfaces. The instantaneous strain rate normal to a ridge is given by

$$S_\perp \equiv \mathbf{n}^T \mathbf{S} \mathbf{n}, \tag{2}$$

where $\mathbf{n}$ is the unit normal vector on the ridge (essentially the eigenvector associated with the negative eigenvalue of the second-derivative matrix) and $\mathbf{S} = [\nabla \mathbf{v} + \nabla \mathbf{v}^T]/2$ is the instantaneous rate of strain tensor at the base time. We also define the two tangential strains,

$$S_{\|1} = \mathbf{e}_1^T \mathbf{S} \mathbf{e}_1, \quad S_{\|2} = \mathbf{e}_2^T \mathbf{S} \mathbf{e}_2, \tag{3}$$

where $\mathbf{e}_1$ and $\mathbf{e}_2$ are the directions of minimal and maximal rate of strain tangent to the ridge surface. (Thus, if we extend in Fig. 7a the ridgeline to a surface that is perpendicular to the plane shown, then the two tangent vectors $\mathbf{e}_1$ and $\mathbf{e}_2$ would lie on this surface.)

As shown in Haller (2001), a ridge of the forward-time DLE field is a hyperbolic LCS if $S_\perp > S_{\|2}$ and $S_\perp > 0$ hold at each point of the ridge for each time. Likewise, a ridge of the backward-time DLE field is hyperbolic if $S_\perp < S_{\|1}$ and $S_\perp < 0$ hold at each point of the ridge for each time. Ridges that do not satisfy the above conditions are classified as parabolic (i.e., of shear type). In Fig. 7a, trajectories arising from hyperbolic- and parabolic-type structures are also shown as black curves with arrows. For trajectories starting on either side of the ridge, if the ridge is repelling and hence $S_\perp > S_\|$, trajectories diverge away from the ridge (the two curved trajectories), whereas if the ridge is a shear such that $S_\perp < S_\|$, the trajectories stay parallel but move with different speed (the two straight trajectories).

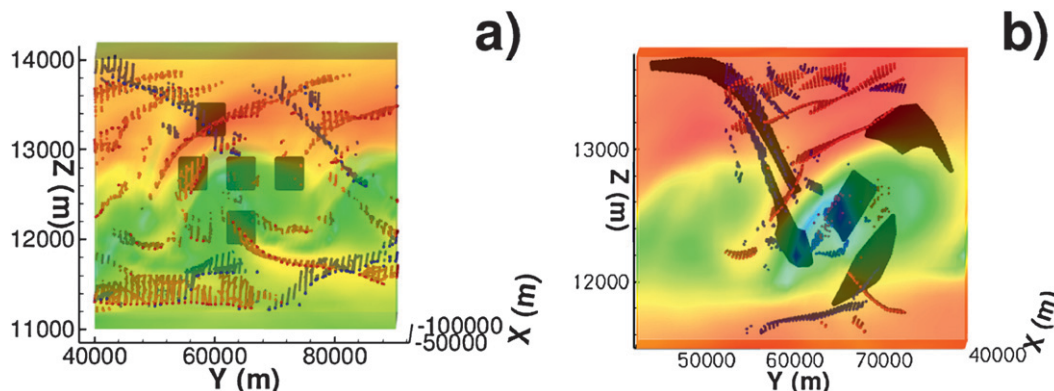Figure 8 shows the evolution of five fluid blobs (the black cubes) along with the LCS. The release locations

FIG. 8. Evolution of five fluid blobs (black cubes) released at several regions of notable DLE features. (a) Original location and associated LCS at 0200 UTC. (b) Later position of fluid blobs and associated LCS at 0300 UTC. The repelling LCS are marked by small red spheres and the attracting LCS are marked by small blue spheres.

are indicated in Fig. 8a, at 0200 UTC, together with the repelling (marked as red spheres) and attracting (marked as blue spheres) structures. As the fluid blobs evolve in time with the LCS, the LCS will attract/repel trajectories, which results in the stretching and folding of these blobs (Fig. 8b). We examine the hyperbolicity criterion described above by comparing with the evolution of these five fluid blobs.

The five fluid blobs are placed at strategic locations. One blob is placed at the vortex center, and four additional blobs are placed in several different regions of interest. The top blob is placed in a hyperbolic core outside of the roll vortex; the center left blob is placed across a repelling surface such that part of it is inside the vortex core; the bottom blob is placed directly below the center blob, at the opening in the DLE field that connects the neighboring vortex; and the center right blob is located in a region where no ridge was extracted based on the algorithm but a weak ridge should be present based on observations in Fig. 7b.

As shown in Fig. 8b, the top, center left, and bottom blobs are all attracted to the blue attracting surfaces, confirming their hyperbolicity [which was independently predicted using Eqs. (2) and (3)]. These attracting surfaces in the roll vortex create specific routes where fluid particles are entrained into the center. At the same time, the red surfaces push these fluid blobs away.

The blob placed at the vortex core indicates that the vortex center is approached as a weak hyperbolic core, itself rotating rapidly. (Notice the slight stretching and strong tilting of the center blob as compared to the other fluid blobs which experience strong stretching and less tilting.) Finally, as we observe from blob deformation in the zonal direction (not shown), all hyperbolic cores experience slight stretching, indicating weak hyperbolicity along the hyperbolic core lines.

5. LCS and atmospheric turbulence: Comparison with balloon measurements

Here we seek to analyze the role of the LCS we found in actual mechanical and optical turbulence observed in situ balloon measurements. Out of the three balloon soundings available on 12 December 2002, only the first two fall in the window of our analysis because of the choice of integration time. The two balloons were released at 0457 and 0657 UTC, both reached the jet stream in about 30 min, and broke at $z \approx 30$ km in about 1 h. Since the evolution of the LCS took place on a much longer time scale compared to the ascending of the balloons, we use the LCS extracted at 0530 and 0730 UTC to represent the Lagrangian topology of the flow over the duration of the balloon flights.

The balloons were released from Bradshaw Army Field (19.47°N, 155.33°W), at an elevation of 1886 m. The soundings record pressure, temperature, relative humidity, and the horizontal wind speed and direction at 2-s intervals. Altitude and ascent rate are computed from the pressure, temperature, and humidity time series. The mean horizontal temperature difference across a horizontal distance of 1 m is also measured and is converted to the refractive index structure constant C_n^2 using the local temperature and pressure (Jumper and Beland 2000), which indicates the level of optical turbulence present in the atmosphere. Optical turbulence is caused by mechanical turbulence in the presence of a temperature gradient. Turbulence within a stratified flow can homogenize temperature in the center of the turbulence, reducing optical turbulence, but also increase temperature gradients on the edges of the mechanical turbulence, enhancing the optical turbulence. The gradient Richardson number Ri can also be estimated based on the in situ balloon data. We look to interpret LCS
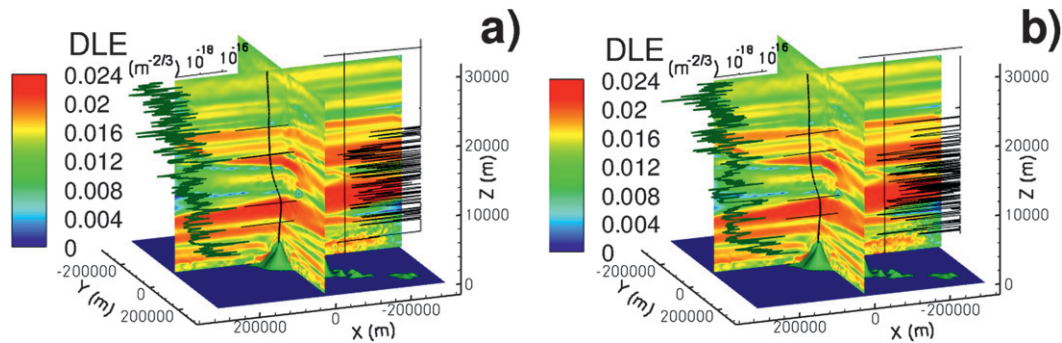
FIG. 9. Comparison between the DLEF field and data collected on thermosonde balloon soundings. (a) First balloon released at 0457 UTC; (b) second balloon released at 0657 UTC. Balloon trajectories are shown in black solid lines, above the topography. The green lines show the refractive index structure constant C_n^2 (m$^{-2/3}$, plotted in log scale). The thin black curves on the right show the gradient Richardson number Ri. The vertical lines indicate locations where Ri = 0. Left of this line we expect convective instability; right of this line, with $0 < Ri < 1$, we expect shear instability. Notice the coincidence of the largest C_n^2 spikes with DLE edges and of small Ri with layers of large DLE.

based on their relation with C_n^2, Ri estimates, and balloon vertical velocity. The first shows how LCS is related to observed optical turbulence; the second shows how LCS is related to observed mechanical turbulence (indicated by shear instability), and the third shows how LCS is related to the helical gravity waves.

Figure 9 gives such comparisons for C_n^2 and Ri for the first two balloon flights. The black solid lines originated from the Big Island are balloon trajectories deduced from the wind measurements and computed altitude. The evolution of these two balloons indicates that they almost ascend vertically below and above the jet, whereas inside the jet core they are carried toward the east by the jet stream. LCS and in situ measurements should be compared along the balloon trajectories.

The green lines in Fig. 9 represent the refractive index structure constant C_n^2 constructed from balloon measurements shown in log scale; large spikes in C_n^2 indicate regions of strong optical turbulence. As we see from Fig. 9, the strongest C_n^2 spikes coincide with the LCS bounding the jet (the black line segments are reference lines of C_n^2 spikes at the location of the balloon trajectory), indicating that the air in the two jet boundaries is homogenized by mechanical turbulence, creating sharp thermal boundaries that house the optical turbulence layers. We also observe smaller spikes of C_n^2 pointing to the boundaries of smaller DLE regions in the jet core (the K-H billows). The black curves on the right of Figs. 9a and 9b, on the other hand, are the estimates of Ri from balloon measurements (filtered to be between −0.1 and 1): regions where $0 < Ri < 1$ indicate shear instability, regions where $Ri < 0$ indicate convective instability, and regions where $Ri > 1$ guarantee stability (Miles 1986). The vertical lines in Fig. 9 indicate Ri = 0 (Ri < 0 to the left of this

line), which separates the two types of instability regions. Stability regions where $Ri > 1$ is also easily seen from the filtering. We observe layers of shear instability in the jet boundary regions and some convective instability regions in the jet core, confirming the strong turbulent motion in these regions bounded by the C_n^2 spikes.

All this suggests that large DLE regions (hyperbolic or parabolic) are the footprints of mechanical turbulence near the jet stream, whereas edges of these regions mark layers of optical turbulence. In particular, mechanical turbulence associated with the overturning of fluid particles in the K-H billows is hyperbolic, whereas mechanical turbulence associated with large wind shear is parabolic. From the one-point balloon measurements, one may draw a false conclusion that the whole layer at the particular altitudes with large C_n^2 spikes is filled with optical turbulence, whereas by observing Figs. 4 and 5b, the height of these thin layers of optical turbulence could very well be variable with the edges of the LCS (i.e., LCS gives a more precise disclosure of the organizing centers of coherent turbulent motions).

Each of the three balloon flights on 12 December 2002 captured three vertical velocity spikes near the tropopause. As observed in McHugh et al. (2008), these velocity spikes correspond to mountain gravity wave peaks and are associated with vertical directional wind shear (the top two velocity anomalies have sudden horizontal wind shifts and hence strong directional wind shear; the lower one has a gradual horizontal wind shift and hence weak directional wind shear). The authors also argued that the WRF does not mimic the large vertical velocities associated with waves because of the damping upper boundary condition imposed.
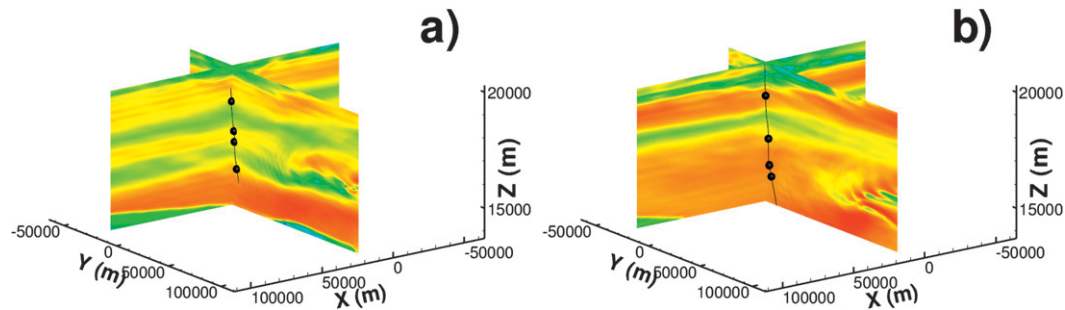
FIG. 10. Large ascent rates in balloon altitudes and the forward-time DLE field. (a) First balloon released at 0457 UTC; (b) second balloon released at 0657 UTC. The black solid lines are the balloon trajectories, and the location of large ascent rates are marked with black spheres. The color contours show the DLEF field on two vertical slices that are close to the balloon trajectories.

The large vertical ascent rates are likely due to insta-bilities associated with directional wind shear (Endlich 1964; Mahalov et al. 2008). Comparisons with DLE based on the WRF data (Fig. 10) show that although vertical velocity is hindered by the upper boundary condition in the WRF, sudden wind shifts are captured by LCS. Figure 10 shows enlargements of the region where the balloons are experiencing large vertical motions (be-tween $z = 14$ km and 20 km).

For the given resolution of the balloon measurements, we observe four vertical velocity anomalies in each flight. The middle two anomalies are close together during the first flight and the lower two during the second flight. The vertical slices correspond to $x = 40$ km and $y = 4$ km, close to the balloon trajectories shown in black solid lines. The locations of the large ascent rates ex-perienced by the balloons are shown as black spheres. In both plots, we see three layers of large LCS, and all large ascent rates that the balloons have experienced happen in these layers. By observing the evolution of fluid blobs starting from these layers (not shown), we find a shift in wind direction that leads to large horizontal stretching of the released fluid blobs. Therefore, although the WRF velocity does not directly produce large vertical velocities at locations of large ascent rates, our DLE analysis does reveal the presence of LCS at those loca-tions because of directional shear.

We do not specifically extract DLE ridges from the subdomains shown in Fig. 10, as the balloon measurements are at a much finer resolution than the WRF velocity field. However, Fig. 10 does suggest that large ascent rates, or peaks in gravity waves, are marked by the red DLE layers. The location of the largest wind shift, cor-responding to the ridges within the red vertical layers in Fig. 10, should be primary candidates for clear air tur-bulence as induced by gravity waves because they are the material structures that experience the most unstable motions.

6. Conclusions

In this paper we have identified Lagrangian coherent structures (LCS) from a direct Lyapunov exponent (DLE) analysis of a three-dimensional atmospheric flow near a subtropical jet stream. The wind field was generated by the Weather Research and Forecasting (WRF) model be-tween 0000 and 1200 UTC 12 December 2002 over Hawaii.

The objective of our study was to identify coherent structures responsible for optical and mechanical tur-bulence in an objective (frame independent) way. We find that frame independence is achieved by the La-grangian methodology. As such, we know the location of different coherent structures in the model data. Beyond frame independence, we also find that resolution of fine detail is an advantage of DLE analysis. Indeed, the struc-tures we have identified are significantly richer in detail than is suggested by the horizontal wind plot (Fig. 3). A further advantage of our approach is sharp edge de-tection, which makes automated structure monitoring algorithms applied to the wind field more effective.

With regard to the particular flow analyzed, our main finding is that the subtropical jet is bounded by two parabolic (shear-type) LCS that are responsible for the creation of optical turbulence. This conclusion is based on a direct comparison of the LCS locations with the highest peaks of the refractive index structure constant C_n^2 available from in situ balloon measurements.

We observe that regions of high values of DLE in the simulation results are coincident with the observed spikes in the balloon ascent data, indicating that neighborhoods of the parabolic LCS are the likeliest candidates for structures that cause shear instability in this model flow.

We have also found that the interior of the subtropical jet is filled with smaller-scale hyperbolic (saddle-type) LCS that create mixing and hence also cause mechanical turbulence. These hyperbolic structures embrace a series of roll vortices, causing entrainment and detrainment in

and out of these vortices. It is well known from previous simulations on K-H instabilities (Fritts et al. 1996) that in an environment with inhomogeneous temperature, such as the flow near a jet stream, mechanical turbulence homogenizes temperature in the interior and creates sharp temperature gradients near the jet boundaries. As a result, the jet stream is bounded by layers of optical turbulence. Optical turbulence is absent if the temperature is homogeneous. In our application of LCS, the exact structures of K-H instability as well as the directional shear bounding the jet stream are revealed, thereby outlining the turbulent landscape of the interaction among different physical processes (skeletons of turbulence).

Recently, some finer-resolution simulations of the jet stream studied here have become available (Joseph et al. 2004; Mahalov et al. 2006). An adaptive grid is used and fine resolution down to several meters is achieved in the jet stream and the clear air turbulence layers. We are planning a DLE analysis of this more recent data to study the fine structures in the clear air turbulence layers and the jet core regions. The objective will be to understand how the inner structure of the jet core contributes to the creation of turbulence patches near the tropopause.

We believe that DLE methods are ideal for feature detection in time-dependent atmospheric flows such as the one considered in this paper. A limitation of the approach is, however, its reliance on well-resolved velocity data. An onboard DLE analysis performed on an aircraft would have, at best, two-dimensional line-of-sight velocity scans obtained from a lidar. A challenging direction of research is the construction of LCS from such limited information. We are currently studying different lidar scanning patterns, some of which appear to provide the required amount of detail for early detection of the LCS responsible for clear-air turbulence.

REFERENCES

Andreassen, O., P. O. Hvidsten, D. C. Fritts, and S. Arendt, 1998: Vorticity dynamics in a breaking internal gravity wave. Part 1. Initial instability evolution. *J. Fluid Mech.,* **367,** 27–46.

Chong, M. S., A. E. Perry, and B. J. Cantwell, 1990: A general classification of three-dimensional flow field. *Phys. Fluids,* **2A,** 765–777.

Clark, T. L., W. D. Hall, R. M. Kerr, D. Middleton, L. Radke, F. M. Ralph, P. J. Neiman, and D. Levinson, 2000: Origins of aircraft-damaging clear-air turbulence during the 9 December 1992 Colorado downslope windstorm: Numerical simulations and comparison with observations. *J. Atmos. Sci.,* **57,** 1105–1131.

Endlich, R. M., 1964: The mesoscale structures of some regions of clear-air turbulence. *J. Appl. Meteor.,* **3,** 261–276.

Fritts, D. C., T. L. Palmer, O. Andreassen, and I. Lie, 1996: Evolution and breakdown of Kelvin–Helmholtz billows in stratified compressible flows. Part I: Comparison of two- and three-dimensional flows. *J. Atmos. Sci.,* **53,** 3173–3191.

Gushchin, V. A., and R. V. Matyushin, 2006: Vortex formation mechanisms in the wake behind a sphere for $200 < \text{Re} < 380$. *Fluid Dyn.,* **41,** 795–809.

Haller, G., 2001: Distinguished material surfaces and coherent structures in three-dimensional fluid flows. *Physica D,* **149,** 248–277.

——, 2002: Lagrangian coherent structures from approximate velocity data. *Phys. Fluids,* **14,** 1851–1861.

——, 2005: An objective definition of a vortex. *J. Fluid Mech.,* **525,** 1–26.

Hunt, J. C. R., and W. H. Snyder, 1980: Experiments on stably and neutrally stratified flow over a model three-dimensional hill. *J. Fluid Mech.,* **96,** 671–704.

Jeong, J., and F. Hussain, 1995: On the identification of a vortex. *J. Fluid Mech.,* **285,** 69–94.

Joseph, B., A. Mahalov, B. Nicolaenko, and K. Tse, 2004: Variability of turbulence and its outer scales in a model tropopause jet. *J. Atmos. Sci.,* **61,** 621–643.

Jumper, G. Y., and R. R. Beland, 2000: Progress in the understanding and modeling of atmospheric optical turbulence. *Proc. 31st AIAA Plasma Dynamics and Laser Conf.,* Denver, CO, AIAA, 1–9.

Koch, S. E., and Coauthors, 2005: Turbulence and gravity waves within an upper-level front. *J. Atmos. Sci.,* **62,** 3885–3908.

Lane, T. P., J. D. Doyle, R. Plougonven, M. A. Shapiro, and R. D. Sharman, 2004: Observations and numerical simulations of inertia–gravity waves and shearing instabilities in the vicinity of a jet stream. *J. Atmos. Sci.,* **61,** 2692–2706.

——, R. D. Sharman, R. G. Frehlich, and J. M. Brown, 2006: Numerical simulations of the wake of Kauai. *J. Appl. Meteor. Climatol.,* **45,** 1313–1331.

Lekien, F., S. C. Shadden, and J. E. Marsden, 2007: Lagrangian coherent structures in *n*-dimensional systems. *J. Math. Phys.,* **48,** 065404, doi:10.1063/1.2740025.

Lu, C., and S. E. Koch, 2008: Interaction of upper-tropospheric turbulence and gravity waves as obtained from spectral and structure function analyses. *J. Atmos. Sci.,* **65,** 2676–2690.

Mahalov, A., M. Moustaoui, and B. Nicholaenko, 2006: Characterization of stratospheric Clear Air Turbulence (CAT) for Air Force platforms. *Proc. HPCMP Users Group Conf.,* Denver, CO, IEEE, 288–295.

——, ——, and ——, 2008: Three-dimensional instabilities in nonparallel shear stratified flows. *Kinet. Relat. Models,* **2,** 215–229.

Mathur, M., G. Haller, T. Peacock, J. E. Ruppert-Felsot, and H. L. Swinney, 2007: Uncovering the Lagrangian skeleton of turbulence. *Phys. Rev. Lett.,* **98,** 144502, doi:10.1103/PhysRevLett.98.144502.

McHugh, J. P., I. Dors, G. Y. Jumper, J. R. Roadcap, E. A. Murphy, and D. C. Hahn, 2008: Large variations in balloon ascent rate over Hawaii. *J. Geophys. Res.,* **113,** D15123, doi:10.1029/2007JD009458.

Miles, J., 1986: Richardson's criterion for the stability of stratified shear flow. *Phys. Fluids,* **29,** 3470–3471.

Okubo, A., 1970: Horizontal dispersion of floatable particles in the vicinity of velocity singularities such as convergences. *Deep-Sea Res.,* **17,** 445–454.

Porter, J. N., D. Stevens, K. Roe, S. Kono, D. Kress, and E. Lau, 2007: Wind environment in the lee of Kauai Island, Hawaii, during trade wind conditions: Weather setting for the Helios Mishap. *Bound.-Layer Meteor.,* **123,** 463–480.

Rotunno, R., and P. K. Smolarkiewicz, 1991: Further results on lee vortices in low-Froude-number flow. *J. Atmos. Sci.,* **48,** 2204–2211.

Shadden, S. C., F. Lekien, and J. E. Marsden, 2005: Definition and properties of Lagrangian coherent structures from finite-time Lyapunov exponents in two-dimensional aperiodic flows. *Physica D,* **212,** 271–304.

——, J. O. Dabiri, and J. E. Marsden, 2006: Lagrangian analysis of fluid transport in empirical vortex ring flows. *Phys. Fluids,* **18,** 047105, doi:10.1063/1.2189885.

Skamarock, W. C., J. B. Klemp, J. Dudhia, D. O. Gill, D. M. Barker, W. Wang, and J. G. Powers, 2005: A description of the Advanced Research WRF version 2. NCAR Tech. Note NCAR/TN-468+STR, 88 pp.

Smolarkiewicz, P. K., and R. Rotunno, 1989: Low Froude number flow past three-dimensional obstacles. Part I: Baroclinically generated lee vortices. *J. Atmos. Sci.,* **46,** 1154–1164.

Weiss, J., 1991: The dynamics of enstrophy transfer in two-dimensional hydrodynamics. *Physica D,* **48,** 273–294.